A Statistical Evaluation of GOES Cloud-Top Properties for Nowcasting Convective Initiation

JOHN R. MECIKALSKI

Atmospheric Science Department, University of Alabama in Huntsville, Huntsville, Alabama

KRISTOPHER M. BEDKA

Cooperative Institute for Meteorological Satellite Studies, Space Science and Engineering Center, University of Wisconsin—Madison, Madison, Wisconsin

SIMON J. PAECH

Atmospheric Science Department, University of Alabama in Huntsville, Huntsville, Alabama

LESLIE A. LITTEN

L3-Communications, ILEX Systems, Eatontown, New Jersey

(Manuscript received 21 August 2007, in final form 18 April 2008)

ABSTRACT

The goal of this project is to validate and extend a study by Mecikalski and Bedka that capitalized on information the Geostationary Operational Environmental Satellite (GOES) instruments provide for nowcasting (i.e., 0–1-h forecasting) convective initiation through the real-time monitoring of cloud-top properties for moving cumuli. Convective initiation (CI) is defined as the first occurrence of a $\geq$35-dBZ radar echo from a cumuliform cloud. Mecikalski and Bedka's study concluded that eight infrared GOES-based "interest fields" of growing cumulus clouds should be monitored over 15–30-min intervals toward predicting CI: the transition of cloud-top brightness temperature to below 0°C, cloud-top cooling rates, and instantaneous and time trends of channel differences 6.5–10.7 and 13.3–10.7 μm. The study results are as follows: 1) measures of accuracy and uncertainty of Mecikalski and Bedka's algorithm via commonly used skill scoring procedures, and 2) a report on the relative importance of each interest field to nowcasting CI using GOES. It is found that for nonpropagating convective events, the skill scores are dependent on which CI interest fields are considered per pixel and are optimized when three–four fields are met for a given 1-km GOES pixel in terms of probability of detection, and threat and Heidke skill scores. The lowest false-alarm rates are found when one field is used: that associated with cloud-top glaciation 30 min prior to CI. Subsequent recommendations for future research toward improving Mecikalski and Bedka's study are suggested especially with regard to constraining CI nowcasts when inhibiting factors are present (e.g., capping inversions).

1. Introduction

The study of Mecikalski and Bedka (2006, hereinafter MB06) demonstrates the use of eight infrared (IR) channels as "interest fields" from the *Geostationary Operational Environmental Satellite-12* (*GOES-12*) for predicting convective initiation (CI) on the 1-km visible (VIS) pixel scale. Within MB06, two unique attributes of the *GOES-12* data stream are manipulated toward efficiently monitoring and tracking convective (i.e., cumulus) clouds in successive 5–15-min resolution images: 1) a "cumulus cloud mask" using a combination of VIS and IR imagery to isolate cumuliform clouds (Berendes et al. 2008) and 2) a cloud-motion-tracking scheme that emphasizes the identification of mesoscale flows associated with cumulus cloud motions (Bedka and Mecikalski 2005; Bedka et al. 2008, manuscript submitted

Corresponding author address: John R. Mecikalski, Atmospheric Science Department, University of Alabama in Huntsville, 320 Sparkman Dr., Huntsville, AL 35805-1912.
E-mail: john.mecikalski@nsstc.uah.edu

DOI: 10.1175/2008MWR2352.1

TABLE 1. The MB06 CI nowcasting interest field criteria and their physical relationship to convective cloud growth and glaciation.

CI interest field	Purpose and resolution	MB06 critical value
6.5–10.7-μm difference (IF1)	4-km cloud-top height relative to upper-tropospheric WV weighting function (Schmetz et al. 1997)	$-35°$ to $-10°$C
13.3–10.7-μm difference (IF2)	8-km cloud-top height assessment/updraft width	$-25°$ to $-5°$C
10.7-μm T_B (IF3)	4-km cloud-top glaciation (Roberts and Rutledge 2003)	$-20° < T_B < 0°$C
10.7-μm T_B drop below 0°C (IF4)	4-km cloud-top glaciation (Roberts and Rutledge 2003)	Within prior 30 min
10.7-μm T_B time trend (IF5 − 15 min, IF6 − 30 min)	4-km cloud-top growth rate/updraft strength (Roberts and Rutledge 2003)	$<-4°$C (15 min)$^{-1}$ ΔT_B (30 min)$^{-1}$ $< \Delta T_B$ (15 min)$^{-1}$
6.5–10.7-μm time trend (IF7)	4-km multispectral cloud growth	$>3°$C (15 min)$^{-1}$
13.3–10.7-μm time trend (IF8)	8-km multispectral cloud growth/updraft width	$>3°$C (15 min)$^{-1}$

to *J. Appl. Meteor. Climatol.*). These techniques isolate only the cumulus convection in geostationary imagery, track moving cumulus convection over time, and identify growing, newly glaciated convective cloud tops. Once cumulus cloud tracking is established using satellite-derived "mesoscale" atmospheric motion vectors (MAMVs), six IR properties (creating eight interest fields) of the 1 km-resolution clouds are monitored and cumulus cloud pixels for which ≥ 7 of the 8 CI interest fields have been satisfied are labeled as having "high" CI potential (~65%) in MB06, assuming an extrapolation of past trends into the future. Details of the eight interest fields, as well as a physical interpretation, are provided in Table 1.

For 2004–06, the MB06 algorithm has been transitioned from a "proof of concept" into a real-time product, one designed for use in broader applications over larger domains. These applications include, in addition to 0–1-h day and night CI nowcasting at 1 km-resolution, CI climatological applications, 0–90-min lightning initiation nowcasting, delineation of surface convergent boundaries (Jay Hanna, NOAA, 2005, personal communication), the monitoring of 0–2-h cloud-top cooling and "CI score" trends, within aviation-safety-based nowcasting systems, specifically the "AutoNowcaster" (Mueller et al. 2003; Mecikalski et al. 2007) and the Corridor Integrated Weather System (CIWS; Wolfson et al. 2004, 2005). Based on the expanded use of the MB06 algorithm, validation and optimization of this algorithm is required, which is the motivation for this study.

Through a detailed visual comparison of CI nowcast fields and composite radar reflectivity imagery, MB06 indicate that the probability of CI detection [i.e., probability of detection (POD)] using the aforementioned methodology is qualitatively ~65% when all eight IR interest fields are used over a range of convective environments. MB06 also suggests that some CI interest fields may have greater skill in nowcasting convective storm development versus others because of the differing spatial and spectral characteristics of each *GOES-12* IR interest field. The results of this study therefore include the development of a more complete and quantitative understanding of the MB06 algorithm in two specific areas: 1) absolute accuracy in terms of POD, false-alarm ratio (FAR), threat score (TS), and the Heidke skill score (HSS); and 2) the relative importance of each interest field in predicting future CI occurrence across a range of convective environments.

All of these goals are accomplished though the combined usage of past, current, and future satellite and radar reflectivity data. The time–space matching of 15–30-min IR trends to radar reflectivity 30–60 min into the future is nontrivial. Nonlinear convective cloud motions as cumuli grow in environments with vertical wind shear, coupled with the nonunique patterns of IR data (as viewed by geostationary satellites) and radar reflectivity fields for the same cloud, require the use of correlation-based pattern matching techniques in order to attain a level of satellite–radar field overlap necessary to develop accuracy statistics. This analysis is described below and constitutes the majority of the effort for this study.

The following section overviews the data analysis, while section 3 presents the methodology. Section 4 describes the main statistical results and an assessment of the importance of each interest field for predicting CI. The paper is discussed and concluded in sections 5 and 6, respectively.

2. Data and preparation

Two primary datasets were utilized within this study, Weather Surveillance Radar-1988 Doppler (WSR-88D) radar reflectivity, and GOES VIS and IR fields. The following sections describe these two datasets and the processing methodologies employed. These were combined to make a dataset consisting of 1 853 265 1-km^2 GOES pixels, for three training events (multiple times on the same day), of which 233 428 cumulus-identified pixels were monitored via the MB06 algorithm. An ad-

TABLE 2. Description of the case events and a brief summary of the soundings in Fig. 2.

Date	Times used	Height of freezing level (meters AGL)	Radar height level used (meters AGL)	Synoptic overview
6 Jul 2004	1400–2200 UTC	3900	2500	Subtropical, with weak shortwave
12 Jul 2004	1400–2200 UTC	4200	2500	Subtropical and upper shortwave
28 Aug 2004	1600–2000 UTC	4000	2500	Subtropical
11 May 2005	2100–2200 UTC	3600	1600	Drier, midwestern summertime

ditional event was used to test the results, as shown below. Table 2 outlines the events used.

a. WSR-88D data

WSR-88D data from National Weather Service station in Hytop, Alabama (KHTX), and Topeka, Kansas (KTWX), were obtained from the National Climatic Data Center (NCDC) level II archive. These data were transformed from the native radar projection to a 1-km resolution Cartesian grid system by the National Center for Atmospheric Research (NCAR) REORDER software package (Oyle and Case 1995). For each CI event, data from the grid level approximately 1–1.5 km below the environmental freezing level (determined from atmospheric soundings) were used. This vertical level was chosen low enough in order to capture the altitude where CI first occurred (at a level where ≥35-dBZ echoes were first observed, as close to the ground as possible), but also to avoid possible effects from bright-band enhancement of radar reflectivity around the freezing level. Additionally, only reflectivity values >10 dBZ were examined to reduce the impact of instrument noise and the appearance of spurious echoes in the analysis.

b. CI interest fields

The *GOES-12* IR CI interest fields computed for the events investigated in this study and the physical interpretations are summarized in Table 1. A pixel that meets seven or eight of the CI interest field criteria represents a growing, newly glaciated cumulus cloud in a pre-CI state (MB06). A more detailed summary of the *GOES-12* instrument and the channels/multispectral techniques used in relation to CI nowcasting is provided in MB06.

The interest fields are remapped to the 1-km resolution Cartesian grid of the WSR-88D data using the Man Computer Interactive Data Access System (McIDAS; Lazzara et al. 1999) software package, instead of allowing them to remain in the native *GOES-12* satellite-viewing projection. As the *GOES-12* satellite views the continental United States from the southeast at a geostationary orbit altitude (~35 786 km), a cumulus cloud pixel is assigned an Earth-relative position that is slightly northwest of its actual location because of parallax. As a result, cumulus cloud features are not initially collocated with their associated radar-observed precipitation echoes in *GOES-12* imagery (Johnson et al. 1994). This parallax error is corrected through geometric relationships that compute the required shift of a given cumulus pixel based on the latitude–longitude of the *GOES-12* satellite nadir point (essentially constant at 0°, 75°W), and the altitude of the cloud feature. The parallax error is greater for higher cloud features at larger distances from the *GOES-12* nadir field of view, and is essentially zero for a clear-sky pixel. A nearby sounding of the atmospheric temperature profile (see below) is used to translate the cloud-top brightness temperature into an altitude above Earth's surface. This process thereby places the satellite-observed cumulus into the best possible alignment with radar reflectivity observations [in lieu of navigation errors induced by the *GOES-12* sensor optics (Menzel and Purdom 1994)].

c. Mesoscale atmospheric motion vectors

MAMVs were used to compute both satellite cloud-top cooling rates and multispectral band differencing trends (as they are in the MB06 algorithm), and help assess the future position of radar echoes (see below). These MAMVs are derived using the Bedka and Mecikalski (2005) algorithm, which is configured such that ageostrophic mesoscale flow components associated with, and induced by, cumuliform clouds can be identified. Bedka and Mecikalski (2005) and MB06 demonstrate the utility of MAMVs in convective storm monitoring and nowcasting (i.e., computing cloud-top temperature and multispectral channel differencing trends for moving cumuli), as well as in depicting divergent flows in the vicinity of convection (see also Jewett 2007). Bedka et al. (2008, manuscript submitted to *J. Appl. Meteor. Climatol.*) establish the relative accuracy of MAMVs as compared with winds obtained by the

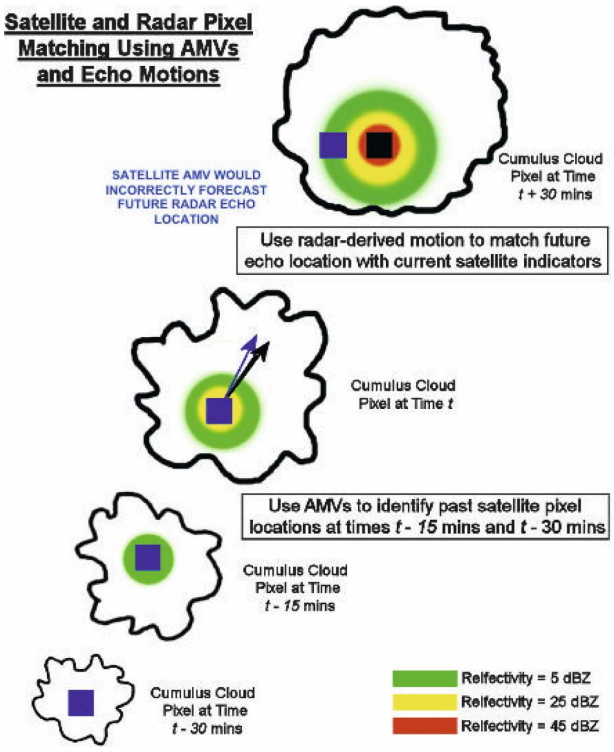

FIG. 1. Justification for non-MAMV advection of infrared cumulus cloud features toward matching future radar echoes.

National Oceanic and Atmospheric Administration's (NOAA) Profiler Network and proximity radiosondes.

In this study, the MAMVs are used to help predict the future position of radar echoes 30–60 min into the future, which constitutes the validation (i.e., did the cumuli predicted to produce a ≥35-dBZ echo reflectivity indeed achieve this?). Clearly, in order to effectively optimize CI nowcasting, one must relate the future evolution of cumulus precipitation structures to the cloud-top diagnostic and growth interest fields observed within real-time satellite imagery.

Use of MAMVs alone in tracking cumuli undergoing CI is challenging given the nonlinear motion patterns of cumulus clouds growing deep into the troposphere (see Fig. 1). MAMVs represent an instantaneous velocity based on the motion of cumulus cloud tops only, which do not necessarily relate well to the motion of the entire cloud. Previous research in the prediction of radar-observed convective storm motion reveals that echoes propagate along the mean 0–6-km flow vector (Johnson et al. 1998), which cannot effectively be computed using MAMVs alone. However, MAMVs provide the spatial–temporal correlation analysis (described below) key first-guess information such that a search radius can be established for performing the radar echo–IR field pattern matching.

d. Matching satellite trends to future radar

As previously noted, use of MAMVs are necessary to advect the IR cloud information to radar echo feature locations 30 min into the future. Figure 1 exemplifies why a purely MAMV-based approach, however, which assumes linear cloud motion over 30–60 min during CI based only on cloud-top winds, may be degraded in environments when the wind shear is significant. Within 1-km resolution radar data, although velocity information exists, it is only radial, and therefore cannot be used. Therefore, the chosen approach was to utilize reflectivity data to calculate the bulk movement of precipitating cloud features. MAMVs do provide a "first guess" for the tracking method, as described below.

Once a cumulus cloud pattern is recognized, two radar views taken 15 min apart are used to calculate movement of precipitating cloud features; this is done as a 10 × 10 pixel region is searched, and if more than one-fourth (i.e., 25 pixels) have >0 dBZ, then a 30-min future radar image is processed. As a level of quality control, the future radar pixel location is cross referenced with the satellite-derived "convective cloud mask" (MB06) computed at this future time to ensure that this precipitation is convectively induced, thereby eliminating the introduction of spurious signals from stratiform clouds. [Note, the current version of the MB06 method uses the convective cloud masking algorithm of Berendes et al. (2008) and this was not employed in this study.] This processing further involves taking a genetic approach, and randomly choosing 10 squares within 30 pixels of the location of the center of the original 10 × 10 box. A least squares fit (used since the characteristics of the cloud are likely to stay nearly the same at 15-min slices) is then done. This procedure can fail if there is significant rotation in the motion of clouds and rainfall echo patterns.

Based on the least squares and genetic approaches, the square with the better average of the two methods is chosen as the centroid (center location) of the echo's future location. Once there is a match, the centroid of each feature is determined, and the vector between the two will be the bulk flow. Given the bulk flow, the future movement using the past two 15-min echoes is estimated. A simple filter is used to remove noise (or sporadic echoes outside the main centroid), and so that the future movement can be optimally predicted. With the present and future (15 and 30 min) echoes now aligned, the pixel-scale CI interest fields can be related to current and future radar echo information.

It is noteworthy that when the centroid and genetic approaches were *not* used, a ~5.5 million pixel dataset

was formed (using additional events) only employing MAMV tracking (given that it was computationally far less expensive to use MAMVs alone in the radar–satellite matching). The results from this larger dataset were qualitatively similar to the finding described below, yet were fraught with many mismatches (as demonstrated in Fig. 1), and the skill scores were often erroneous, when compared to analysis by a human expert (i.e., pixel-to-pixel matching). These skills did become comparable to those obtained using the centroid and genetic approaches *only* when substantial preprocessing and editing (prestatistical analysis) were performed to effectively weed out the mismatched pixels. In the end, we chose not to use this large, initial dataset because of the likelihood that we were skewing the results toward unrealistically high POD, TS, and HSS, and low FAR scores. In retrospect, because these initial results were qualitatively similar, we feel good that those obtained below are robust.

e. Case event description

Four CI events compose our dataset from which the accuracy assessments are determined (see Table 2). Three of these events compose the training dataset. These were within a humid subtropical environment over north Alabama and south-central Tennessee. One other event used to evaluate the analysis is for a drier convective environment over Kansas. It is understood that the IR interest fields used within the MB06 algorithm will vary somewhat across convective environments (i.e., convective regimes). The reasons for this includes the height of the freezing altitude, the amount of dry air above developing cumulus clouds, and the available water vapor in the boundary layer supporting cloud development (i.e., the subsequent in-cloud humidity). Therefore, analyzing cases in a variety of convective environments enhances the robustness of the validation statistics.

The three training events were chosen because of their proximity to the HTX Doppler radar within the *GOES-12* view (Table 2), and possess environments in which moisture for CI was not a factor limiting cumulus growth and rainfall. The 6 and 12 July, and 28 August 2004 CI events were also selected as the synoptic-scale forcing was relatively weak, storm motions were relatively slow ($\leq$15 m s^{-1}), and both cloud and storm motions were generally uniform along one velocity vector regardless of cloud size (i.e., cumuli in both pre- to post-CI state). Weak vertical shear and the lack of a deep dry layer within the sounding (see Figs. 2a–c) also helped dictate use of these days' data as storm structures were relatively simple, with a limited tilt in updrafts and therefore a higher likelihood that satellite and radar fields could be optimally collocated in the vertical. In essence, strong vertical shear would have likely reduced our ability to collocate radar and satellite fields for the same storm. The 11 May 2005 CI case represents an event with stronger synoptic-scale dynamic forcing, and was a significant convective event with numerous outflow interactions, to contrast the other three subtropical cases; the sounding from Topeka at 1200 UTC 11 May 2005 is shown in Fig. 2d.

3. Methodology

At this point in the process, the satellite CI interest fields and current/future radar reflectivity information are known, assuming satellite/radar data were properly tracked both backward and forward in time. When these techniques are applied to the four cases mentioned above, a total of over 1.8 million 1-km^2 GOES pixels collocated with WSR-88D level II radar data were compiled (each day comprising approximately 12–18 individual 30-min nowcasting periods), with each pixel possessing values for all eight CI interest fields, as well as current and future radar reflectivity information. It is noteworthy that pixels that possessed 0 interest fields (within their respective "critical" ranges; i.e., nothing in GOES suggested developing, growing cumulus) are included in this dataset, such that proper statistics may be assessed from pixels with radar echoes present but no IR indicators of CI.

Principal component analysis (PCA) was also performed as a means of estimating information content and redundancy in these IR data for CI nowcasting.

a. Skill determination

Four measures of forecasting skill (i.e., POD, FAR, TS, and HSS) are used to evaluate the MB06 CI nowcast products. The POD and FAR are defined as in Wilks (2006, 264–265): POD = $a/(a + c)$; FAR is defined similarly as FAR = $b/(a + b)$. The TS and HSS are also as in Wilks (2006, 263 and 266, respectively), where TS = $a/(a + b + c)$, and HSS = $2(ad - bc)/[(a + c)(c + d) + (a + b)(b + d)]$.

In these, POD is the fraction of those occasions when the forecast event occurred (CI in this case) in which it was also forecast to occur (a), relative to all observations of CI ($a + c$). FAR is the fraction of "yes" forecasts that turned out to be incorrect (b) relative to all non-CI events ($a + b$). Here, c is the number of events that were not forecast but where CI was observed, and d is the number of events that were not forecast and were not observed. The TS (also called the

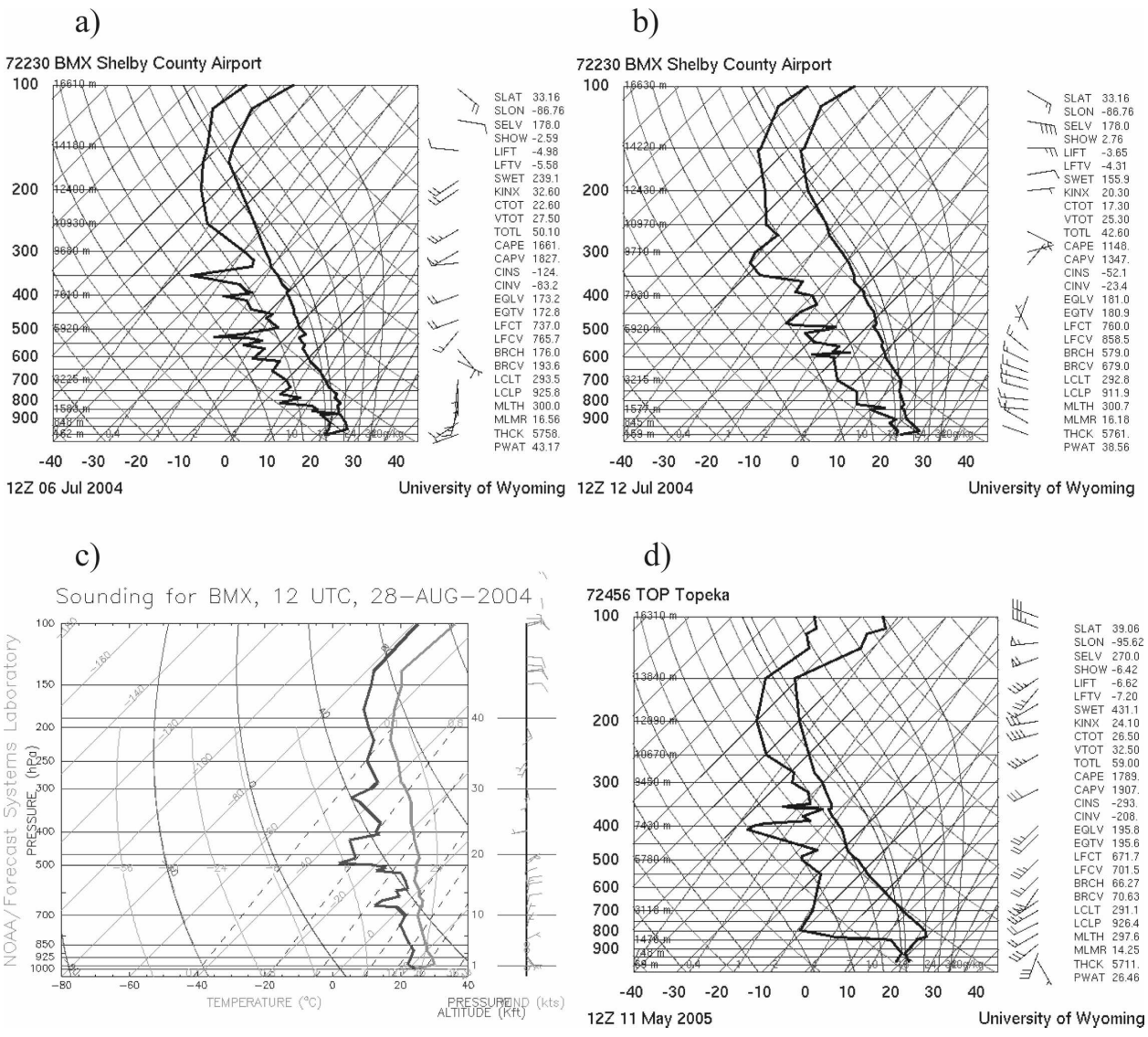

FIG. 2. Representative soundings for CI events used within this study (see Table 2): the Birmingham, AL, sounding at (a) 1200 UTC 6 Jul 2004, (b) 1200 UTC 12 Jul 2004, and (c) 1200 UTC 28 Aug 2004; and (d) the Topeka, KS, sounding at 1200 UTC 11 May 2005.

"critical success index") represents the number of correct forecasts of CI divided by the total number of occasions in which the event was forecast and/or observed. The HSS (Heidke 1926) is a more robust skill score that summarizes the square contingency tables. The HSS represents a reference accuracy measure, and is the proportion correct (forecasts) that would be achieved by random forecasts that are statistically independent of the observations, and is the product of $p(e_y)p(o_y)$ and $p(e_n)p(o_n)$. Here, p represents "probability," e_y and e_n are yes and no events, respectively, and o_y and o_n are observations of yes and no observations of the event. Therefore, $p(e_y)$ represents the probability of a yes forecast of CI, and $p(e_y)p(o_y)$ represents the probability of a yes forecast by chance (Wilks 2006). An HSS of 1 implies a perfect forecast, and an HSS of 0 implies a forecast equivalent to a reference forecast, which in this case means random chance.

Given the eight interest fields, two methods have been developed for presenting the results. The first is simply to determine and present what IR interest fields are most and least associated with CI at a given pixel. The second involves a more complicated procedure of determining the optimal set of fields for nowcasting CI, for all possible combinations of fields, from one single field to all eight per pixel, based on the optimization of skill scores (i.e., highest POD, TS, and HSS, and the lowest FAR). These results are presented in Tables 3–6.

TABLE 3. Maximum PODs as a function of convective initiation interest field numbers, and combinations, per GOES (1 × 1 km) pixel. Here the interest fields are abbreviated IF followed by the number, as in Table 1. In this table, the combination of (rows 2–8) *all or some* of the fields need to be present to obtain the POD scores shown. The particular field(s) that contribute(s) to the highest skills are denoted with an "X".

No.	IF1	IF2	IF3	IF4	IF5	IF6	IF7	IF8	POD
1		X							0.8825
2		X				X			0.9781
3		X				X		X	0.9916
4		X		X	X	X			0.9979
5	X	X		X		X	X		0.9981
6	X	X	X	X		X	X		0.9981
7	X	X	X	X	X	X	X		0.9981
8	X	X	X	X	X	X	X	X	0.9981

TABLE 4. Minimum FARs as a function of convective initiation interest field numbers and combinations per GOES (1 × 1 km) pixel as in Table 3. See Table 3 and text for further explanation. The particular field(s) that contribute(s) to the highest skills are denoted with an "X".

No.	IF1	IF2	IF3	IF4	IF5	IF6	IF7	IF8	FAR
1				X					0.6939
2			X	X					0.7061
3	X		X	X					0.7239
4	X		X	X			X		0.7361
5	X		X	X	X		X		0.7397
6	X		X	X	X		X	X	0.7416
7	X	X	X	X	X		X	X	0.7446
8	X	X	X	X	X	X	X	X	0.7456

TABLE 5. Maximum TS as a function of convective initiation interest field numbers and combinations per GOES (1 × 1 km) pixel as in Table 3. See Table 3 and text for further explanation. The particular field(s) that contribute(s) to the highest skills are denoted with an "X".

No.	IF1	IF2	IF3	IF4	IF5	IF6	IF7	IF8	TS
1		X							0.2575
2		X		X					0.2595
3		X	X	X					0.2608
4	X	X	X	X					0.2601
5	X	X	X	X			X		0.2569
6	X	X	X	X		X	X		0.2549
7	X	X	X	X		X	X	X	0.2544
8	X	X	X	X	X	X	X	X	0.2543

b. Principal component analysis

PCA is used here to discern the relative amount of information within the IR data of a GOES pixel (i.e., within each of the eight CI interest fields). PCA, also known as empirical orthogonal function (EOF) analysis, is a common method used to reduce a dataset from a large number of variables to one in which only a few new variables are required to describe the necessary and important information (Wilks 2006). Because of the commonness of use of PCA within atmospheric analysis, we refer the reader to Wilks (2006), as well as more classical treatments by Jolliffe (2002) and Preisendorfer (1988), for an overview of this technique.

For the purposes of this analysis, we are interested in determining which of the eight interest fields contain a relative amount of important information in comparison to others, or, which combination of indicators is important; it is unlikely that all of the eight fields will contain the same level of information on future CI, with some likely containing redundant information (goal 2 of this paper). In the following section, the PCA for this dataset, and the skill scores for the MB06 method, are described.

4. Results

a. Skill analysis

The statistical analysis was performed as a means of addressing the first objective of this paper (measures of nowcast skills and uncertainty in the GOES CI methodology). This analysis consists of determining, for all "cumulus" pixels in the dataset, the POD, FAR, TS, and HSS as a function of ≤8 interest fields. Tables 3–6 present these results, respectively. These tables present the skills as a function of the number of interest fields per GOES pixel that are in range (see Table 1) and evaluate how to optimally nowcast with only one field, all the way to using all eight fields. Specifically, for these tables, the field(s) that combined to form the highest skills are those listed, given all possible combinations of one–eight fields (per pixel). The particular field(s) that contribute(s) to the highest skills are denoted with an "X" in the tables.

The far right-hand side of Table 6 lists the contingency table results that the TS and HSS skills (in Tables 3–6) were developed from. This dataset consisted of 233 428 cumulus pixels, and 8946 of these were "CI pixels" in which a ≥35-dBZ echo developed out of a growing cumulus cloud (i.e., out of a cumulus-cloud pixel). It needs to be noted that the MB06 algorithm operates on all cumulus pixels, and hence any of the CI interest fields can be "within range" for any GOES cumulus pixel. As an example, Table 4 shows that the transition of cloud-top temperature from above to below 0°C within the past 30 min (IF4; see Table 1) provides the lowest FARs at ~69% (see top row), which implies that IF4 occurs for the fewest number of cumulus pixels that never initiated into deep convection.

TABLE 6. Maximum HSS as a function of convective initiation interest field numbers and combinations per GOES (1 × 1 km) pixel as in Table 3. The contingency table values *a*, *b*, *c*, and *d*, are also provided, which apply to Tables 3–6. A total of 233 428 GOES pixels were evaluated to obtain the contingency results. The particular field(s) that contribute(s) to the highest skills are denoted with an "X".

No.	IF1	IF2	IF3	IF4	IF5	IF6	IF7	IF8	HSS	*a*	*b*	*c*	*d*
1		X							0.3752	7895	21 720	1051	202 762
2		X		X					0.3775	8062	22 116	884	202 366
3		X	X	X					0.3785	8250	22 683	696	201 799
4	X	X	X	X					0.3766	8478	23 650	468	200 832
5	X	X	X	X			X		0.3715	8671	24 805	275	199 677
6	X	X	X	X	X		X		0.3679	8683	25 190	263	199 292
7	X	X	X	X		X	X	X	0.3670	8929	26 154	17	198 328
8	X	X	X	X	X	X	X	X	0.3669	8929	26 163	17	198 319

In forming these statistics, we have evaluated all 255 possible combinations of eight fields per pixel, with the idea that some or all fields may be present. For example, in the case of four fields, we logically consider two conditions: 1) whether *all* four are "in range" (a logical "and" condition), and 2) whether *any* four are in range (a logical "or" condition) for a given pixel. The data in Tables 3–6 are for the logical-or case as a means of maximizing skills for various combinations; we will only discuss the second set of results: those in which we demand that any one field be in range for a pixel. The first condition is much more restrictive, and provides significantly lower skill scores.

From Table 3 it is seen that use of the instantaneous 13.3–10.7-μm channel difference (IF2) provides the highest POD at 88.3%; stated another way, when this channel difference is within the −25- to −5-K range, there is an 88.3% probability that CI (as we have defined it) will occur within the following 30 min for the moving cumulus as observed by GOES. The POD increases to 97.8% when the 30-min time change in 10.7 μm (IF6) is used together IF2. The PODs peak at 99.8% when five or more fields are considered together, in particular, fields 1–2, 4, and 6–7. This would suggest that inclusion of IF3, IF5, and IF8 may not add much toward increasing POD when single-pixel scoring is performed. (Future work is addressing issues associated with errors in computing IF5 and IF6, caused by incorrect tracking of growing cumulus.) When we insist on all fields being in range (the logical and condition) the PODs maximize for one field just as shown in Table 3, but decrease to only 9.3% when all eight fields are considered per pixel. The interpretation of this is that all eight fields are in range only 9.3% of the time when CI is observed 30 min into the future, but, when all eight fields are in range, we find that the probability for CI is quite high (over 90%) for that pixel. Surprisingly, the FARs remain above 65% when requiring that all eight fields be simultaneously in range.

Results derived from processing these data also suggest these following single-field frequencies when CI was observed, for a given interest field being "within range" for a pixel (i.e., *a* in the contingency table divided by 8946): IF1 75.1%, IF2 88.3% (as shown in Table 3), IF3 44.9%, IF4 23.1%, IF5 54.2%, IF6 73.0%, IF7 60.4%, and IF8 48.1%. When CI was predicted but not observed (i.e., *b*/8946), the following results were obtained: the single-field results were 67.0% for IF1, 82.8% for IF2, 36.4% for IF3, 17.9% for IF4, 55.4% for IF5, 75.3% for IF6, 59.1% for IF7, and 46.3% for IF8. Therefore, IF4 was not in range when CI was nowcast only ~18% of the time.

As stated above, Table 4 shows that (single interest field) FAR scores are minimized when IF4 is used alone, at 69.4%. IF4 signifies glaciation; without this indicator being available for a given cumulus cloud, CI would not be likely, except when "warm rain" microphysical processes are dominant (Pruppacher and Klett 1998, chapter 9; see below regarding the weaknesses of the MB06 method with respect to convection occurring in various environments). When using additional fields, we find that the FARs increase to approximately 74%–75%. We speculate that these relatively large FARs may infer a limit to satellite-based CI nowcasting, and suggests that other additional information will be required to constrain the results, for example, the location and strength of a capping inversion that very often inhibits CI. It also suggests that errors in cumulus tracking, and those associated with 4-km IR resolution, provide current-day limits to the MB06 method (i.e., IR data are at scales above the "cumulus cloud scale," namely ~1 km).

Table 5 and 6 show the TS and HSS skills, respectively. Several interesting features are apparent. First, threat scores are highest (26.1%) when 3 interest fields are used (IF2, IF3, and IF4), with the HSS maximizing at 37.9%, for the same three fields. The TS and HSS in these two tables, in which we require *some or all* of the fields to be within range, are otherwise nearly constant. The contingency table numbers (*a*, *b*, *c*, and *d*) in Table

6 show that up to 8929 of the 8946 are nowcasted via this method, with 17 pixels (the "*c*" value) being missed entirely. Again, it is surmised that this implies that additional nonsatellite information may be needed to significantly improve the MB06 method for TS and HSS skills. We feel however, that it does not suggest that some CI interest fields provide limited information toward nowcasting CI, especially in light of the PCA results to be discussed below (Table 7).

Some additional analysis was performed in which we considered the individual cases of IF1–8 being within range (not shown). This analysis suggests that for those pixels that possessed exactly a given amount of IFs in range, the TS reaches ~34% for the IF6–7 pixels (comprising IF1, IF2, IF3, IF4, IF6, and IF8; IF7 contributes to the IF7 case), while the HSS reached a maximum at ~50% for the IF6–7 pixels (with the same fields being important as for the TS results). One problem with this analysis is that the number of "hits" for nowcasting CI decrease significantly from 7895 to 833 as the number of fields used in the nowcast increase from 1 to 8, exemplifying the low PODs seen for the logical and results (i.e., ~9.3%).

The relationship of the results in Tables 3–6 to physical cumulus cloud behavior observed by GOES suggests the following: 1) Incorporation of the 8-km-resolution 13.3-μm channel (as interpolated to the 1-km radar data resolution for this application) provides high value in detecting and observing cloud growth of the larger cumulus clouds (i.e., the larger updrafts). In other words, when a cumulus cloud produces a strong signal in the 13.3-μm channel it implies an updraft of considerable size—between 4 and 8 km in width. We surmise then that as updraft widths increase there is increased likelihood of CI over the next hour (larger updrafts are more likely to persist for longer time periods). This is a fortuitous outcome of this study, and suggests that with any geostationary satellite, use of lower-resolution data (approximately 4–8 km) may be valuable for nowcasting the CI process. 2) Cloud-top glaciation, via the transition of the 10.7-μm IR T_B from above to below freezing, is key for maximizing PODs, TSs, and HSSs. The reasoning for this was discussed above. 3) Cloud-top temperature (IF3) are valuable for increasing TS and HSS skills. 4) The 6.5–10.7-μm IR T_B difference is more important than the 15-min trend in this field, as well as cloud-top cooling rates, for monitoring in-cloud updrafts toward the occurrence of CI. This channel difference is highest for deep cumulus extending into middle troposphere levels, and hence those that have likely broken a capping inversion. This result was not anticipated given the results of Roberts and Rutledge (2003). The 15-min cooling rate (versus the 30-min rate) may be a poorer discriminator of CI given that many "towering" cumuli can possess cloud-top cooling rates consistent with those found by Roberts and Rutledge, albeit never grow far enough to eventually produce rainfall. We suspect that many cumuli that grow rapidly (i.e., towering cumulus) never achieve CI due to the presence of capping inversions, hence resulting in lower skill score results.

Tables 3–6 also suggest the following "hierarchy" of interest field usage for nowcasting the occurrence of a ≥35-dBZ radar echo given information from the *GOES-12* instruments (the second objective of this study): 1) 13.3–10.7-μm T_B difference (IF2), 2) the transition from above to below 0°C as measured by the 10.7-μm channel (IF4), 3) cloud-top temperature (10.7 T_B; IF3), 4) the 6.5–10.7-μm T_B difference (IF1), and 4) the time trend in 6.5–10.7-μm T_B difference (IF7). The 15- and 30-min cloud-top cooling rates measured through the 10.7-μm channel values (IF5 and IF6) appear next in line for contributing to CI nowcasting value. As shown, TS and the HSS are both maximized when using four fields (IF1–IF4). The statistical results highlight the need to understand when certain IR fields will not add value to the CI nowcast, and that conditional (or intelligent) scoring has value over simply using all eight fields per pixel. Tables 3–6 also illustrate an interesting aspect of the MB06 method: when fewer than eight interest fields are used in the scoring, *each pixel can possess a unique set of skill scores*, depending on which fields happen to be within range. As an example, if a pixel's score is 6 (say if IF1, IF3, IF4, IF6, IF7, and IF8 are all in range), then it has a unique set of skill scores in comparison with another pixel with a different set of six fields within range. Use of Tables 3–6 therefore allows for more certainty when applying the MB06 algorithm since the method's skill is understood when a prescribed set of fields is chosen.

As a means of demonstrating various approaches to per-pixel scoring (hence the variations in nowcast accuracy), several examples are shown. Results for 2 times during the 6 July 2004 event (1702 and 1715 UTC), and at 2015 UTC 11 May 2005, are seen in Figs. 3a–f, 4a–f, and–5a–f, respectively. Shown panels a and b are current (the time when the CI nowcast was made) and future (the time when the CI nowcast becomes valid: 30–60 min into the future) radar reflectivity, the MB06 scoring approach with seven–eight of eight indicators within the range (labeled "scoring-based nowcast" in panels c), the MB06 methodology in which *any* four of eight interest fields are within their respective ranges (labeled "SATCAST4 nowcast" in panels d), the MB06 methodology in which *all* eight interest fields are within their respective ranges (labeled "SATCAST8

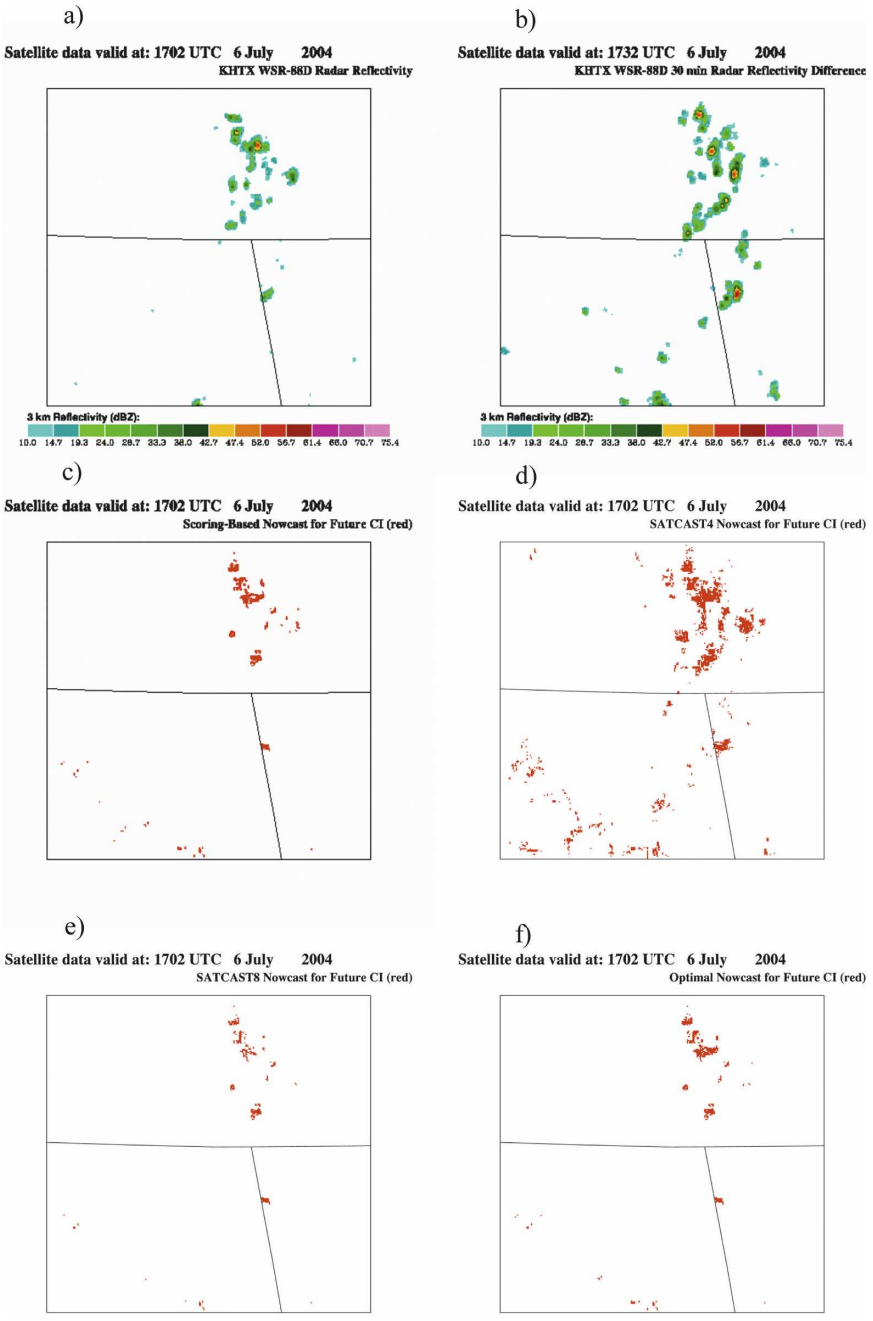

FIG. 3. Comparison of nowcasting methods for a case found at 1702 UTC 6 Jul 2004. Shown are the Hytop, AL (KHTX), WSR-88D reflectivity at a 2-km height at (a) 1702 UTC and (b) the positive differences in reflectivity at 1732 UTC, i.e., the reflectivity at 1732 UTC minus that at 1702 UTC, with all negative differences removed from the plot. Here (a) is the initial time radar reflectivity (t_0), and (b) is the time $t = t_0 + 30$ min. (c) The CI nowcasting method as developed in MB06 (labeled scoring-based nowcasting, i.e., seven or eight of eight fields are within range). (d) For comparison, the scoring approach in which any four of the eight interest fields are within range. (e) The MB06 method in which all eight fields are within range, and (f) one approach (labeled optimal) as described in the text in which IF2, IF1, IF6, and IF4 are used together. The nowcasts in (c)–(f) were created at 1702 UTC, and are valid between 1702 and 1802 UTC. See text for discussion.

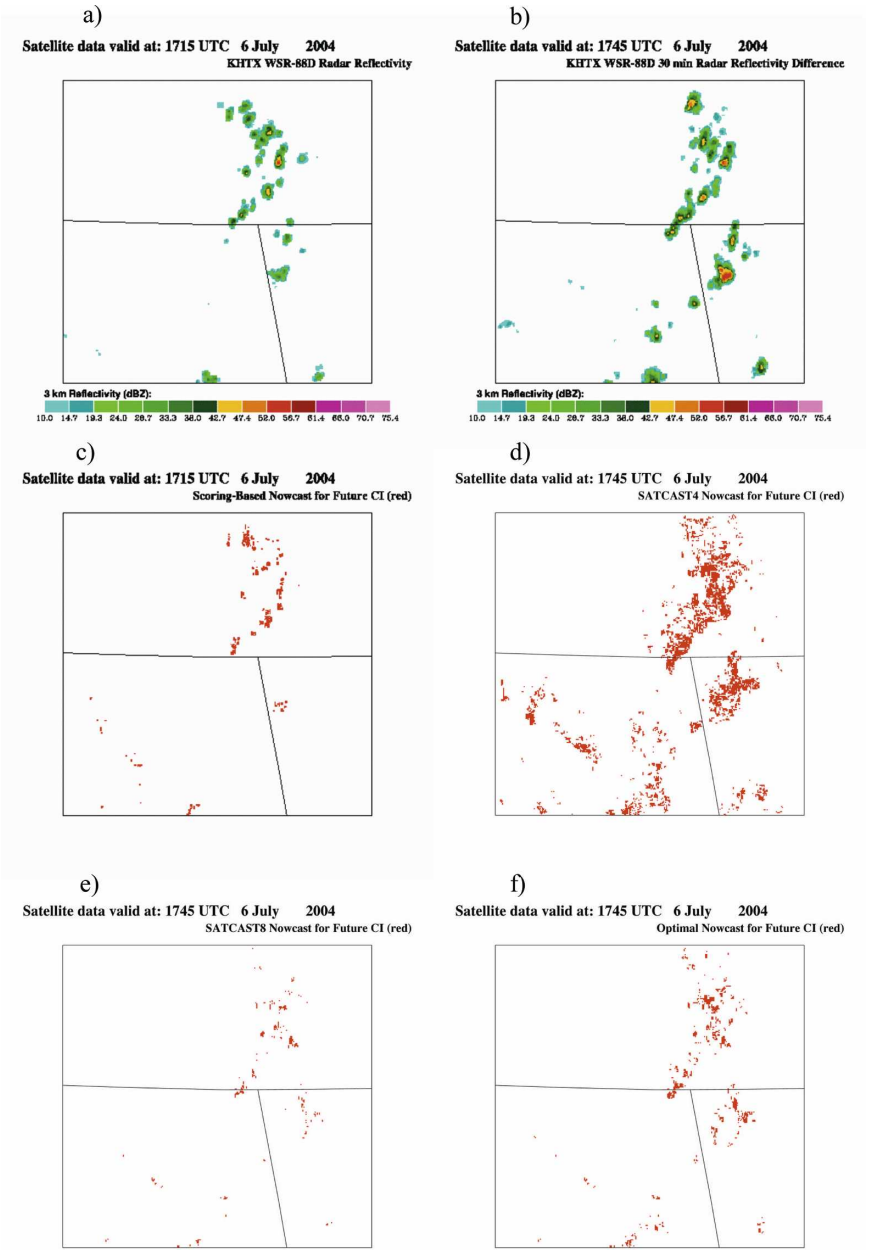

FIG. 4. As in Fig. 3, but the initial time (t_0) is (a) 1715 UTC 6 Jul 2004, and the following 30-min difference time is (b) 1745 UTC 6 Jul 2004. (c)–(f) Both forecasts were created at 1715 UTC, and are valid between 1715 and 1815 UTC.

nowcast" in panels e), and one approach (labeled "optimal" in panels f) using only fields IF2, IF1, IF6, and IF4 together.

From these figures, several things can be seen and understood: 1) using the MB06 method with *any* four fields within the range leads to relatively poor skill results, as seen in Figs. 3d, 4d, and 5d, with significant overpredictions (high PODs) of CI; these overpredictions of CI have been quantified as nearly a factor of 3. 2) Using the MB06 method with seven or eight of eight fields mimics the optimal images. 3) Figures 3f, 4f, and 5f show a reduction in the number of cumulus pixels forecasted to experience CI within the 0–1-h timeframe by approximately 5%–10%, relative to the 7–8 scored MB06 method. 4) The MB06 method with eight of eight fields within range provides the most conservative estimate of new CI. From these figures, the use of simple (unconditional scoring) suggests that the MB06 method with all eight IR indicators in range provides nearly the highest quality nowcasts, and the use of scoring with

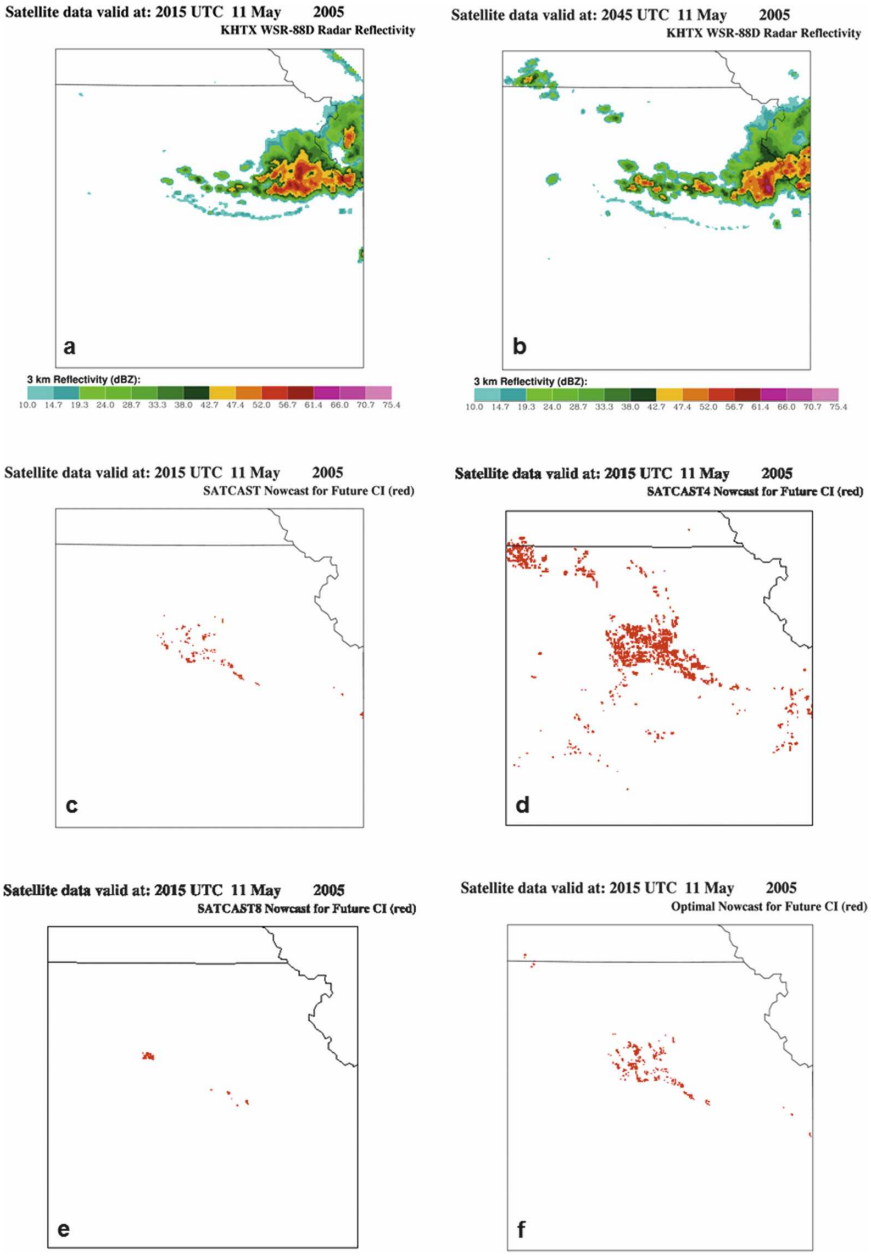

FIG. 5. As in Fig. 3, but the initial time (t_0) is (a) 2015 UTC 11 May 2005 over Topeka for WSR-88D reflectivity at a 2-km height, and the following 30-min difference time is (b) 2045 UTC 11 May 2005. (c)–(f) Both forecasts were created at 2015 UTC, and are valid between 2015 and 2115 UTC. Note that this event demonstrates how these methods compare in regions distant from the initial test domain over AL and southern middle TN.

seven interest fields (i.e., with IF5 not included) is one way of optimizing this algorithm for either maximizing the TS and the HSS.

b. *Principal component analysis*

The results of the PCA analysis for this dataset are shown in Table 7. These results pertain to pixels meeting the CI definition. In this analysis, only seven interest fields could be assessed; IF4 is a binary field, which does not work well within PCA.

Within the lower triangular matrix shown in Table 7, significant correlations (above |0.7|) are in boldface. Notable high correlations exist between IF2 and IF1 (positive), IF3 and IF1 (negative), IF3 and IF2 (nega-

TABLE 7. PCA results for eight CI interest fields. The first eight rows show the correlation matrix as a lower-triangular matrix. For this analysis, because IF4 was a binary (yes or no) condition, we could not use it within the PCA. Based on the analysis shown in the last eight rows, PC1–3 are considered to contain useful information, and, more important, none of the seven CI interest fields contain a significant amount of redundant information on forecasting the occurrence of CI using GOES IR data. Here, "ExVar" is explained variance. Boldface numbers show significant correlations and value as described in text.

Correlations	IF1	IF2	IF3	IF5	IF6	IF7	IF8
IF1	1.000	—	—	—	—	—	—
IF2	**0.8581**	1.000	—	—	—	—	—
IF3	**−0.9388**	**−0.8690**	1.000	—	—	—	—
IF5	−0.2411	−0.3304	0.2818	1.000	—	—	—
IF6	−0.4403	−0.4989	0.5143	0.5976	1.000	—	—
IF7	0.1405	0.2246	−0.1358	**−0.9323**	−0.5029	1.000	—
IF8	0.0914	0.3405	−0.0892	**−0.7743**	−0.3654	**0.7826**	1.000
ExVar							
PC1	**23.745**	**12.318**	**−33.025**	−7.552	**−16.327**	4.048	2.986
PC2	**10.425**	1.758	**−11.616**	**22.017**	**22.970**	**−17.277**	**−13.936**
PC3	7.712	5.807	−1.729	**−17.353**	**34.192**	**15.330**	**17.877**
PC4	−1.057	−28.687	−11.201	−17.045	5.090	10.407	−26.514
PC5	−39.710	6.427	−28.009	−4.775	4.812	−9.567	6.700
PC6	−6.859	34.038	7.016	−5.932	2.323	14.112	−29.721
PC7	−7.123	−5.950	−9.345	33.245	−0.824	39.048	4.465
PC	Eigenvalue		% Variance				
1	396.87		67.64				
2	122.21		20.83				
3	42.57		7.26				
4	11.59		1.98				
5	8.93		1.52				
6	2.66		0.454				
7	1.89		0.322				

tive), IF7 and IF5 (negative), IF8 and IF5 (negative), and IF8 and IF7 (positive). Static channel differences between the 6.5–10.7-, 13.3–10.7-, and 10.7-μm channels are strongly related to cloud-top temperature as obtained from IF3. We also note with surprise that IF5 and IF6 are only correlated at ~0.6, which seems consistent with the results of Tables 3–6. IF7 and 8 are also highly correlated, which likely follows from the high correlation seen between IF1 and IF2.

Assessment of the principal components and explained variance tables provides an interesting conclusion. 1) Principal component 1 (comprising IF1, IF2, IF3, and IF6, each with explained variance >10) alone describes 67.64% of the variance for forecasting CI from these data, with component 2 (comprising IF1, IF3, and IF5–8) adding another 20.83% (totaling 88.47%) and component 3 (comprising IF5–8) adding another 7.26% (totaling 95.73%). 2) If principal components 1–3 are considered valuable together, then analysis of the explained variances between all IFs shows that *all of the seven fields contribute some level of useful information to CI nowcasting*. It was also determined above the relevance of cloud-top glaciation (IF4) to the CI process. This implies that use of fewer than seven IFs can set skill limits to the scoring approach used in MB06, as demonstrated in Figs. 3d, 4d, and 5d.

5. Discussion and uncertainty analysis

Provided the results above, we will now discuss the analysis uncertainties. This research has shown that unspecified 1–8 scoring using MB06 may not be optimal versus use of only 3–4 (scoring using IF1, IF2, IF3, or IF4 per pixel) or all 8 at once per pixel. However, the MB06 method should provide reasonable skill over a range of convective environments, especially in nontropical conditions.

It should be noted that the basis for all accuracy calculations and skill scores is the requirement that cloud tracking is robust. Use of the MB06 algorithm where cumulus tracking is unavailable or of poor quality causes the skill scores to suffer dramatically. For this work, we realize that the MAMVs (used in MB06) are only as accurate as the retrieval algorithm, and in cases of significant vertical wind shear [approximately ≥ 10 m s^{-1} (1 km)$^{-1}$] we can expect accuracies to fall off in our CI predictions, both spatially and temporally.

There are several limitations and sources for error in the above validation approach. These will be discussed in turn. The first is that there is certainly a level of mismatch between GOES and WSR-88D data (see Fig. 1). Figure 6 (also shown in MB06) illustrates how mismatch can occur because of the physical difference in

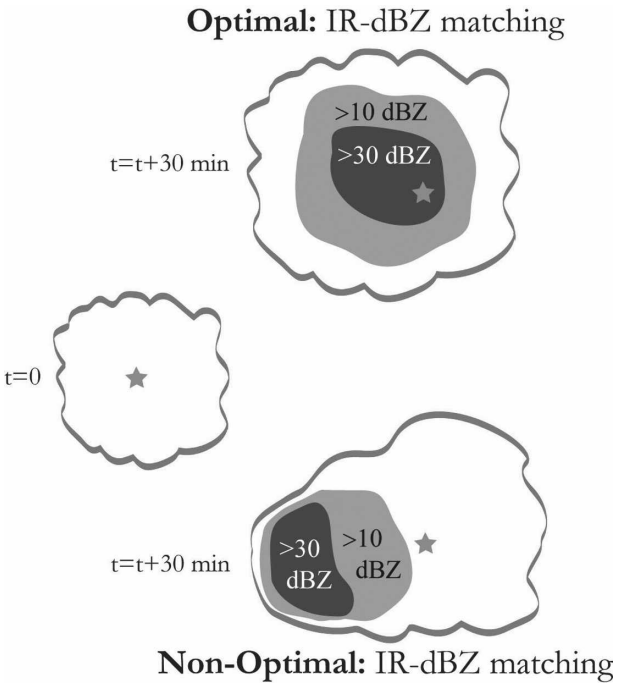

FIG. 6. Schematic that demonstrates the problems associated with correlating a radar echo with a satellite-viewed cloud in the IR portion of the spectrum. (left) The initial size and shape of a cumulus at the time of a CI nowcast ($t = 0$). The star represents a pixel where at least seven CI interest field criteria are met (i.e., a CI nowcast pixel). (top right) "The optimal": the radar echo (dBZ) maximum corresponds well with the cloud-relative location of the CI nowcast pixel 30 min later. This correspondence results from relatively low vertical shear and simplistic internal cumulus dynamics, similar to that found in a summertime "air-mass" thunderstorm over the southern United States. (bottom right) "The nonoptimal": the CI nowcast pixel and radar echoes are poorly related in space. This results from high vertical shear and complex internal cumulus dynamics, causing the precipitation to shift away from the cloud-relative location of satellite-derived CI signatures (i.e., center of the cloud). This situation can occur in association with a squall line or supercell-type thunderstorm (Browning 1964) and leads to "error" within the methods described, despite the fact that our methods have "nowcast" the presence of a precipitating cumulus cloud at a 30-min lead time.

area coverage between the GOES IR signal and WSR-88D radar echo for a given cloud. This can be quantified for cases when a cumulus cloud consumes less than a 4 km × 4 km GOES IR pixel (i.e., 16 1-km-resolution pixels), in essence, when the cumulus updraft is smaller than 4 km^2; recall that the 4-km data are used at 1-km resolution in MB06, to retain the full capabilities the visible data provide in terms of resolution for identifying cumulus clouds. For example, if a cumulus cloud feature is 3 versus 4 km^2, the cloudy region occupies 56.25% within a 4-km-resolution GOES 10.7-μm pixel and 43.75% is from the clear air. The cloud signal reaching the GOES IR sensor, being averaged over the pixel area, decreases to 25% and 6.25% for 2- and 1-km^2 updraft/cumulus, respectively (versus a 4-km^2 pixel). Clearly this is a source of error in this method and, to be more specific, in the values obtained for each CI interest field by GOES. It is suspected that this contributes to the relatively low TS and HSS, depending on what type of scoring is used.

Other sources of mismatch between GOES and WSR-88D could also result from poor cloud/radar pixel tracking using MAMVs and the parallax view correction procedure. It is felt that the MAMV error is limited to environments possessing significant vertical wind shear, which was not the case in the four events used in this analysis (see also, the discussion in MB06). Errors due to incorrect parallax corrections, albeit a possible source of mismatch between GOES and WSR-88D data, are constrained by the viewing geometry of the GOES satellite for clouds at 33°–36°N; implementation of our parallax corrections are limited to the maximum error possible from this source: ~4 km or ~1 GOES IR pixel. We feel very confident in our implementation of the parallax correction, especially given the aforementioned quality control checks that ensure that locations of radar echoes correspond to satellite observed cumulus clouds.

6. Conclusions

This project extended a previous study that demonstrated the use of GOES VIS and IR data for estimating 0–1-h CI through the real-time monitoring of cloud-top infrared properties by assessing the explicit contributions of all satellite interest fields to CI predictability. The previously reported accuracy from MB06 for 1-km^2 CI nowcasts was ~65% in terms of POD. This study represents a sound quantification of this accuracy, and of the relative importance of a given IR interest field to CI predictions.

Other end results of this research are 1) measures of accuracy (i.e., FAR, POD, TS, and HSS) skills, and uncertainty in the GOES CI methodology, and 2) a report on the relative importance of each interest field to forecasting CI using GOES.

The maximum POD for the MB06 method (with eight of eight fields in range) is ~99.8%, with FAR skills minimized at ~69%. The TS and HSS maximize at 26.1% and ~38%, respectively, when three fields are scored. Use of <8 fields results in "conditional skills," which may be used as well within this algorithm, and that implies considerable variability in per-pixel scores depending on which IR fields are within range. Figures 3–5 demonstrate these skills for one example of conditional scoring in which IF2, IF1, IF6, and IF4 are used,

for three events. This results in more cumulus pixels highlighted as having high CI potential, as compared to the MB06 procedure with seven–eight or eight scores. Tables 5 and 6 suggest that using IF2, IF3, or IF4 in MB06 alone maximize the TS and HSS skills, hence maximizing POD at ~99% and keeping the FARs relatively low.

Describing these results in terms of cumulus cloud behavior as observed by GOES suggests the following: 1) incorporation of the 8-km-resolution 13.3-μm channel provides high value in detecting and observing cloud growth of the larger cumulus clouds (i.e., as updraft widths increase there is increased likelihood of CI over the next hour; larger updrafts survive longer); 2) the transition from above to below 0°C as measured by the 10.7-μm channel (i.e., cloud-top glaciation); 3) cloud-top temperature (colder cumulus imply CI); 4) the 6.5–10.7-μm T_B difference (i.e., cumulus growing into middle tropospheric levels implies a capping inversion is no longer present); and 5) the time trend in 6.5–10.7-μm T_B difference. The 15- and 30-min cloud-top cooling rates measured through the 10.7-μm channel values are important as well for contributing to CI nowcasting value, as suggested by Roberts and Rutledge (2003). The statistical results highlight the need to understand when certain IR fields will not add value to the CI nowcast, and that conditional scoring has more value over simply using all eight fields per pixel. Tables 3–6 also illustrate an interesting aspect of the MB06 method, namely that when fewer than eight interest fields are used in the scoring, *each pixel possesses a unique set of skill scores*, depending on which fields happen to be within range. Use of those combinations presented in the tables, as well as use of eight of eight fields, precludes some of this uncertainty.

New research is under way to optimize the MB06 algorithm for various convective "regime" environments. Specifically, it is recognized that in cases where the warm rain microphysical process dominates (i.e., in marine environments), this algorithm will likely underpredict the occurrence of $\geq$35-dBZ echoes. Also, in particularly dry environments (e.g., the intermountain western United States and the Mexican Plateau), it is believed that the MB06 procedure will significantly overpredict CI as evaporation of rainfall is high (and rainfall efficiencies are low), leading to cases where a 35-dBZ radar echo is never attained at the surface. Based on the high FARs with the MB06 method, it is also a focus of new research to develop methods that help constrain the satellite-based CI estimates by including environmental factors known to inhibit CI (e.g., the intensity of the capping inversion). Such information can readily be obtained from operational numerical weather prediction models.

Performing analysis using geostationary and polar-orbiting satellites, with IR sensors that possess more channels than GOES, is also occurring. For example, the Moderate Resolution Imaging Spectroradiometer (MODIS) and the European Spinning Enhanced Visible and infrared Imager (SEVIRI) on the Meteosat Second Generation (MSG; *Meteosat-8* and *Meteosat-9*) instrument possess 37 and 12 channels, respectively. Using SEVIRI data, for example, may provide up to an additional ~10 interest fields (capitalizing on the 0.8-, 1.6-, 3.8-, 6.2-, 7.3-, 8.7-, and 12.0-μm channels, along with time trends of difference channels like 8.7–10.8 μm) will improve the MB06 methodology for monitoring cloud-top microphysics important in the precipitation development process (see Rosenfeld et al. 2008).

It is important that any implementation of satellite "interest fields" within a complex decision-support system (e.g., the "AutoNowcaster"; Wilson et al. 1998; Mueller et al. 2003), the Met Office's Generating Advanced Nowcasts for Deployment in Operational Land Surface Flood Forecast (GANDOLF; Pierce and Hardaker 2000), the Central American Flash Flood Guidance System (CAFFG; see online at www.hrc-lab.org/right_nav_widgets/realtime_caffg/index.php), and the Corridor Integrated Weather System (CIWS; Wolfson et al. 2005) as developed at the Massachusetts Institute of Technology, requires knowledge of *both* the accuracy and uncertainty in the estimates. We hope these results can assist in the use of satellite-based CI nowcasting procedures within such systems.

Acknowledgments. This research was supported by NASA New Investigator Program Award Grant NAG5-12536 and NASA Advanced Satellite Aviation Weather Products (ASAP) Award 4400071484. The authors thank Rita Roberts [NCAR Research Applications Laboratory (RAL)] and Cindy Mueller (NCAR RAL) for research suggestions that guided this work in its very early stages. We thank the satellite-derived winds group within the Cooperative Institute for Meteorological Satellite Studies (CIMSS) at the University of Wisconsin for their help and guidance setting up the satellite-derived AMV software within our nowcasting system. The authors greatly appreciate the help that Dr. Daniel Lindsey (NOAA/Cooperative Institute for Research in the Atmosphere) offered in terms of discussion, analysis, and project review, which significantly improved the paper's quality. One additional anonymous reviewer also contributed toward improving the paper's value.

REFERENCES

Bedka, K. M., and J. R. Mecikalski, 2005: Application of satellite-derived atmospheric motion vectors for estimating mesoscale flows. *J. Appl. Meteor.,* **44,** 1761–1772.

Berendes, T. A., J. R. Mecikalski, W. M. Mackenzie Jr., K. M. Bedka, and U. S. Nair, 2008: Convective cloud identification in daytime satellite imagery using standard deviation limited adaptive clustering. *J. Geophys. Res.,* **113,** D20207, doi:10.1029/2008JD010287.

Browning, K. A., 1964: Airflow and precipitation trajectories within severe local storms which travel to the right of the winds. *J. Atmos. Sci.,* **21,** 634–639.

Heidke, P., 1926: Berechnung des erfolges und der gute der windstarkvorhersagen im sturmwarnungsdienst. *Geogr. Ann.,* **8,** 301–349.

Jewett, C. P., 2007: Retrieval of convective momentum fluxes using geostationary satellite data. M.S. thesis, University of Alabama in Huntsville, Huntsville, AL, 92 pp.

Johnson, D. B., P. Flament, and R. L. Bernstein, 1994: High-resolution satellite imagery for mesoscale meteorological studies. *Bull. Amer. Meteor. Soc.,* **75,** 5–33.

Johnson, J. T., P. L. MacKeen, A. Witt, E. D. Mitchell, G. J. Stumpf, M. D. Eilts, and K. W. Thomas, 1998: The storm cell identification and tracking algorithm: An enhanced WSR-88D algorithm. *Wea. Forecasting,* **13,** 263–276.

Jolliffe, I. T., 2002: *Principal Component Analysis*. 2nd ed. Springer, 487 pp.

Lazzara, M. A., and Coauthors, 1999: The Man computer Interactive Data Access System: 25 years of interactive processing. *Bull. Amer. Meteor. Soc.,* **80,** 271–284.

Mecikalski, J. R., and K. M. Bedka, 2006: Forecasting convective initiation by monitoring the evolution of moving convection in daytime GOES imagery. *Mon. Wea. Rev.,* **134,** 49–78.

——, and Coauthors, 2007: Aviation applications for satellite-based observations of cloud properties, convective initiation, in-flight icing, turbulence, and volcanic ash. *Bull. Amer. Meteor. Soc.,* **88,** 1589–1607.

Menzel, W. P., and J. F. Purdom, 1994: Introducing GOES-I: The first of a new generation of geostationary operational environmental satellites. *Bull. Amer. Meteor. Soc.,* **75,** 757–781.

Mueller, C., T. Saxen, R. Roberts, J. Wilson, T. Bentancourt, S. Dettling, N. Oien, and J. Yee, 2003: NCAR Auto-Nowcast System. *Wea. Forecasting,* **18,** 545–561.

Oyle, D., and M. Case, 1995: REORDER: A program for gridding radar data. Installation and use manual for the UNIX version, NCAR Atmospheric Technology Division, Boulder, CO, 19 pp.

Pierce, C. E., and P. J. Hardaker, 2000: GANDOLF: A system for generating automated nowcasts of convective precipitation. *Meteor. Appl.,* **8,** 341–360.

Preisendorfer, R. W., 1988: *Principal Component Analysis in Meteorology and Oceanography*. Elsevier, 425 pp.

Pruppacher, H. R., and J. D. Klett, 1998: *Microphysics of Clouds and Precipitation*. Kluwer Academic Publishers, 954 pp.

Roberts, R. D., and S. Rutledge, 2003: Nowcasting storm initiation and growth using *GOES-8* and WSR-88D data. *Wea. Forecasting,* **18,** 562–584.

Rosenfeld, D., W. L. Woodley, A. Lerner, G. Kelman, and D. T. Lindsey, 2008: Satellite detection of severe convective storms by their retrieved vertical profiles of cloud particle effective radius and thermodynamic phase. *J. Geophys. Res.,* **113,** D04208, doi:10.1029/2007JD008600.

Schmetz, J., S. A. Tjemkes, M. Gube, and L. van de Berg, 1997: Monitoring deep convection and convective overshooting with Meteosat. *Adv. Space Res.,* **19,** 433–441.

Wilks, D. S., 2006: *Statistical Methods in the Atmospheric Sciences.* 2nd ed. Academic Press, 627 pp.

Wilson, J. W., N. A. Crook, C. K. Mueller, J. Sun, and M. Dixon, 1998: Nowcasting thunderstorms: A status report. *Bull. Amer. Meteor. Soc.,* **79,** 2079–2099.

Wolfson, M. M., and Coauthors, 2004: Tactical 0-2 hour convective weather forecasts for FAA. Preprints, *11th Conf. on Aviation, Range, and Aerospace Meteorology,* Hyannis, MA, Amer. Meteor. Soc., 3.1. [Available online at http://ams.confex.com/ams/pdfpapers/81242.pdf.]

——, W. Dupree, R. Boldi, C. Wilson, K. Calden, R. Johnson Jr., and P. Bieringer, 2005: Tactical 0-2-hour convective weather forecasts for the FAA. *World Weather Research Program Symp. on Nowcasting and Very Short Range Forecasting,* Toulouse, France, WWRP, 182 pp.